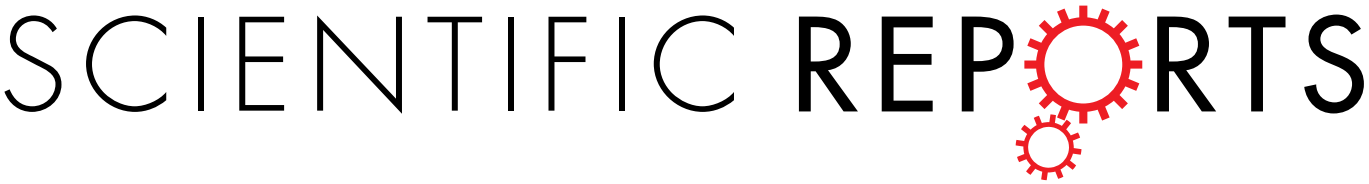

OPEN

Superconductivity and Charge Density Wave in $ZrTe_{3-x}Se_x$

Xiangde Zhu[1,2], Wei Ning[1], Lijun Li[2], Langsheng Ling[1], Ranran Zhang[1], Jinglei Zhang[1], Kefeng Wang[2,†], Yu Liu[3,‡], Li Pi[1,4], Yongchang Ma[2,5], Haifeng Du[1], Minglian Tian[1,4], Yuping Sun[1,3,4], Cedomir Petrovic[2] & Yuheng Zhang[1,4]

Received: 14 February 2016
Accepted: 09 May 2016
Published: 02 June 2016

Charge density wave (CDW), the periodic modulation of the electronic charge density, will open a gap on the Fermi surface that commonly leads to decreased or vanishing conductivity. On the other hand superconductivity, a commonly believed competing order, features a Fermi surface gap that results in infinite conductivity. Here we report that superconductivity emerges upon Se doping in CDW conductor $ZrTe_3$ when the long range CDW order is gradually suppressed. Superconducting critical temperature $T_c(x)$ in $ZrTe_{3-x}Se_x$ ($0 \leq x \leq 0.1$) increases up to 4 K plateau for $0.04 \leq x \leq 0.07$. Further increase in Se content results in diminishing T_c and filametary superconductivity. The CDW modes from Raman spectra are observed in $x = 0.04$ and 0.1 crystals, where signature of $ZrTe_3$ CDW order in resistivity vanishes. The electronic-scattering for high T_c crystals is dominated by local CDW fluctuations at high temperatures, the resistivity is linear up to highest measured $T = 300$ K and contributes to substantial in-plane anisotropy.

Charge density wave (CDW) and superconductivity (SC), both Fermi surface instabilities and low-temperature collective orders in solids, are commonly believed to compete with each other[1,2]. Recently, dynamic CDW fluctuations have also been discussed in copper oxide superconductors[3] in connection with quantum critical transition between CDW and superconductivity. CDW favors low dimensional systems, especially transition metal (M) MX_2 and MX_3 chalcogenides (X represents S, Se and Te)[1,4]. Among them, $ZrTe_3$ is of interest since its crystal structure (Fig. 1a) is quasi-two dimensional (2D), yet it contains two quasi-one dimensional (1D) trigonal prismatic $ZrTe_6$ chains with inversion symmetry along the b-axis[5]. From the view along c-axis (Fig. 1b), the top Te2/Te3 atoms form a rectangular network with the distances of 0.279/0.310 nm along the a axis and 0.393 nm along the b-axis. The first principle calculation gives evidence that the electron-type band (Te2/Te3 $5p_x$ in origin) provides the major contribution, whereas the contribution of the partially filled hole-type band that originates in Te1 $5p_y$ and Zr $4d_{y^2}$ orbitals is minor at the Fermi surface[5]. Angular resolved photoemission (ARPES) demonstrates that CDW originates from the Te2/Te3 $5p_x$ band[6].

$ZrTe_3$ features not only a CDW transition temperature (T_{CDW}) ~63 K with a CDW vector $\vec{q} \approx \left(\frac{1}{14}; 0; \frac{1}{3}\right)$ but also a nearly isotropic in-plane and quasi-two-dimensional (2D) electronic transport[5,7,8]. There is a filamentary SC in a stoichiometric single crystal with higher onset of T_c for a-axis from resistivity measurement than for b-axis[5,9]. Heat capacity data suggest that SC transitions in $ZrTe_3$ are successive from filamentary-to-bulk with local pair fluctuations above T_c; SC phase first condenses into filaments along a-axis, becoming phase coherent below 2 K[9]. Pressure(P), intercalation, and disorder can tune $ZrTe_3$ into bulk SC with suppression of CDW order[10–12].

Here we provide evidence for the pronounced upper critical field $H_{c2}(T)$ anisotropy and emerging 1D electronic transport along the $ZrTe_6$ chain-direction b axis in $ZrTe_{3-x}Se_x$ ($0 \leq x \leq 0.1$). The $H_{c2}(T)$ anisotropy and new Raman modes suggest coexistence of local CDW modes and enhanced superconducting $T_c(x)$ in $ZrTe_{3-x}Se_x$.

[1]High Magnetic Field Laboratory, Chinese Academy of Sciences and University of Science and Technology of China, Hefei 230031, China. [2]Condensed Matter Physics and Materials Science Department, Brookhaven National Laboratory, Upton, New York 11973, USA. [3]Key Laboratory of Materials Physics, Institute of Solid State Physics Chinese Academy of Sciences, Hefei 230031, China. [4]Collaborative Innovation Center of Advanced Microstructures, Nanjing 210093, China. [5]School of Materials Science and Engineering, Tianjin University of Technology, Tianjin 300384, China. [†]Present address: CNAM, Department of Physics, University of Maryland, College Park, Maryland 20742, USA. [‡]Present address: Condensed Matter Physics and Materials Science Department, Upton NY 11973, USA. Correspondence and requests for materials should be addressed to C.P. (email: petrovic@bnl.gov) or Y.H.Z. (zhangyh@hmfl.ac.cn)

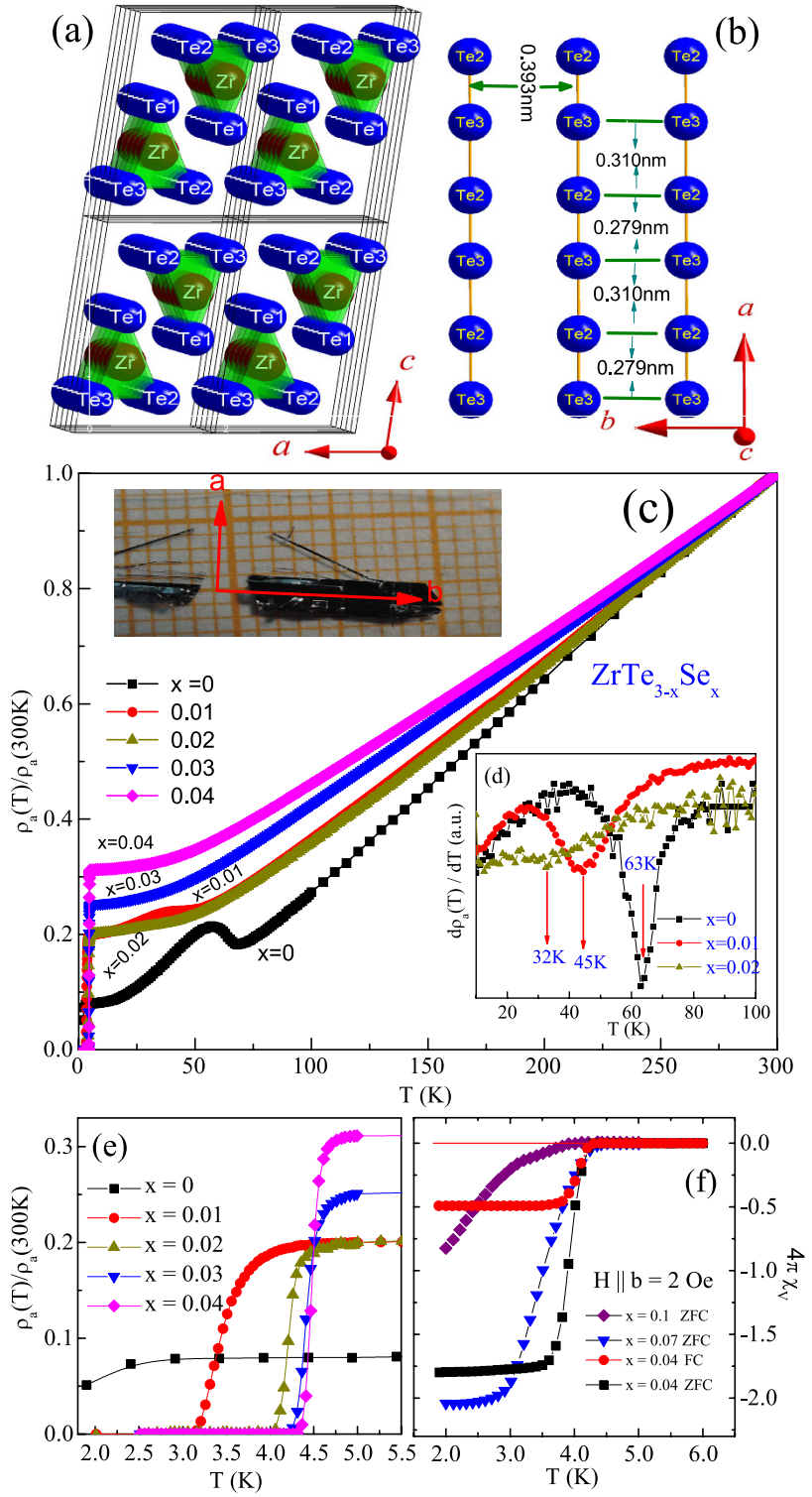

Figure 1. (**a**) Crystal structure of $ZrTe_3$. (**b**) Top Te2/Te3 rectangular network layer viewed from *c*-axis. The quasi 1D $ZrTe_6$ chains run along the *b*-axis, with the shortest Zr-Zr distance and Te1-Te1 distance of 0.393 nm. Solid line denotes the alternately spaced Te2/Te3 chain. (**c**) Temperature dependence of normalized $\rho_a(\rho_a/\rho_a(300\,K))$ for $ZrTe_{3-x}Se_x$. The inset shows a typical photograph of cleaved $ZrTe_{3-x}Se_x$ crystal. Some fibers along *b*-axis can be observed. (**d**) The T_{CDW} is determined from the dips in the differential curves of $\rho_a/\rho_a(300\,K) - T$ (shown in the inset). Solid rectangular, circle and triangle represent x = 0, 1% and 2%, respectively. The arrows mark the T_{CDW}. (**e**) Low temperature $\rho_a/\rho_a(300\,K) - T$. Superconducting T_c is determined as the midpoint of the superconducting transition. (**f**) The temperature dependence of magnetic susceptibility (χ) measured for $ZrTe_{2.96}Se_{0.04}$, $ZrTe_{2.93}Se_{0.07}$, and $ZrTe_{2.9}Se_{0.1}$. The applied magnetic field(H) is 2 Oe and parallel to the *b* axis of crystal.

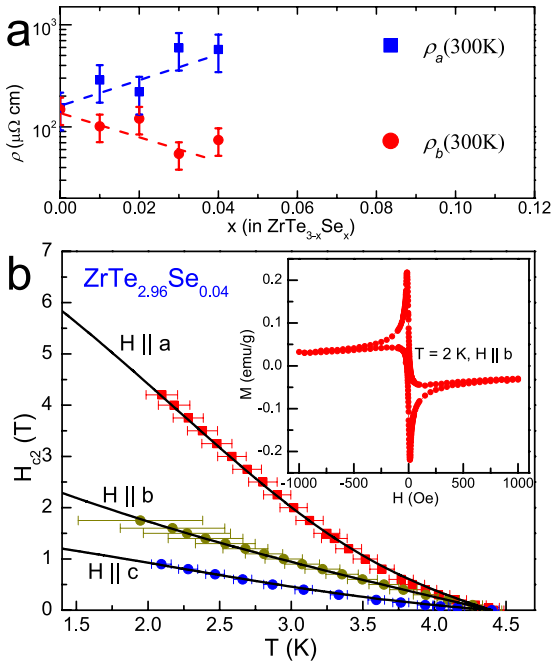

Figure 2. (**a**) The log-plots of ρ_a(solid square) and ρ_b(solid circle) versus Se doping content. (**b**) The temperature dependence of the upper critical field (H_{c2}) (determined as the midpoint of the superconducting transition; the error bars are the difference from the 10% and 90% resistivity drop) of $ZrTe_{2.96}Se_{0.04}$ for H || a, H || b and H || c. The solid lines represents the fitts of the two band model (see text). Inset shows the magnetic hysteresis ($M-H$) loop for $ZrTe_{2.96}Se_{0.04}$ measured at 2 K.

Results

Normalized ρ_a [ρ_a/ρ_a(300 K)] [Fig. 1(c)] shows that the CDW anomaly is suppressed with increasing Se content. The T_{CDW} [Fig. 1(d)] decreases whereas the bulk superconductivity sets in [Fig. 1(e,f)]. For $x \leq 0.04$, as shown in Fig. 1(e), the superconducting transition temperature (T_c) determined from the $\rho_a(T)$ curves tends to increase, and transition width decreases. With increasing Se content $x \geq 0.04$, [Fig. 1(f)], somewhat lower $T_c = 4$ K is observed for $x = 0.07$, and the superconducting transition becomes wide and filamentary for $x = 0.1$ with $T_c \sim 3.1$ K. $ZrTe_{2.96}Se_{0.04}$ shows typical behaviour of a type-II superconductor, whose field cooling (FC) χ is smaller than in zero field cooling process (ZFC) [Fig. 1(f)].

The ρ_a and ρ_b are almost identical to each other in $ZrTe_3$ (x = 0), however with increasing Se content x, room temperature ρ_a tends to increase, while ρ_b tends to decrease [Fig. 2(a)]. This indicates that $ZrTe_{3-x}Se_x$ becomes highly conducting along b-axis in the normal state. If $ZrTe_{3-x}Se_x$ is an anisotropic superconductor with dominant quasi-1D (super)conductivity along the b-axis, upper critical field along b axis ($H_{c2}\|b$) should be larger than $H_{c2}\|a$, according to the single band anisotropic Ginzburg-Landau theory since

$$\Gamma_{ij} = m_{ii}^*/m_{jj}^* = H_{c2}\|j/H_{c2}\|i \sim \sqrt{\rho_i/\rho_j} \quad (1)$$

To confirm this, we choose the $ZrTe_{2.96}Se_{0.04}$ crystal where the ratio of $\rho_a(T)/\rho_b(T)$ is about 10 at 300 K [Fig. 2(a)]. The magnetic hysteresis ($M-H$) loop for $ZrTe_{2.96}Se_{0.04}$ [Fig. 2(b) inset] confirms that it is a typical type-II superconductor with some electromagnetic granularity. In $ZrTe_{2.96}Se_{0.04}$, $H_{C2}(T)\|a > H_{C2}(T)\|b > H_{C2}(T)\|c$ relation can be observed [Fig. 2(b)]. This is in contrast to the b-axis quasi-1D conductivity in the normal state suggesting multiband effects and/or additional factors that can contribute to mass tensor anisotropy. The upward curvature of H_{c2}-T curves implies that the multiband effects should be considered.

The $H_{C2}(T)$ for the two-band BCS model with orbital pair breaking is[13]:

$$a_0[\ln t + U(h)][\ln t + U(\eta h)] + a_2[\ln t + U(\eta h)] + a_1[\ln t + U(h)] = 0, \quad (2)$$

$$U(x) = \psi(1/2 + x) - \psi(1/2), \quad (3)$$

where $t = T/T_c$, $\psi(x)$ is the digamma function, $\eta = D_2/D_1$, D_1 and D_2 are band 1 and band 2 diffusivities, $h = H_{c2}D_1/(2\phi_0 T)$, and $\phi_0 = 2.07 \times 10^{-15}$ Wb is the magnetic flux quantum. $a_0 = 2w/\lambda_0$, $a_1 = 1 + \lambda_-/\lambda_0$, and $a_2 = 1 - \lambda_-/\lambda_0$, where $w = \lambda_{11}\lambda_{22} - \lambda_{12}\lambda_{21}$, $\lambda_0 = (\lambda_-^2 + 4\lambda_{12}\lambda_{21})^{1/2}$, and $\lambda_- = \lambda_{11} - \lambda_{22}$. Interband coupling in two bands is given by λ_{12} and λ_{21} whereas λ_{11} and λ_{22} are intraband coupling constants in band 1 and 2, when $D_1 = D_2$, this simplifies to the one-band model orbital pair breaking in the dirty limit[14]. Dominant intraband (interband) coupling is obtained for $w > 0 (w < 0)$. The fits to the multiband model using $\lambda_{i,j}$ $i, j = 1, 2$ in Table 1 are excellent [solid lines in Fig. 2(b)]. Overall, the fitting results indicate dominant intraband coupling[15,16]. Interestingly, the

H_{c2}‖	η	λ_{11}	λ_{12}	λ_{21}	λ_{22}
a	0.098	0.60	0.25	0.25	0.80
b	0.124	0.60	0.50	0.50	0.60
c	0.145	0.60	0.25	0.25	0.80

Table 1. Citting parameters of H_{c2} for $Cu_{0.05}ZrTe_3$.

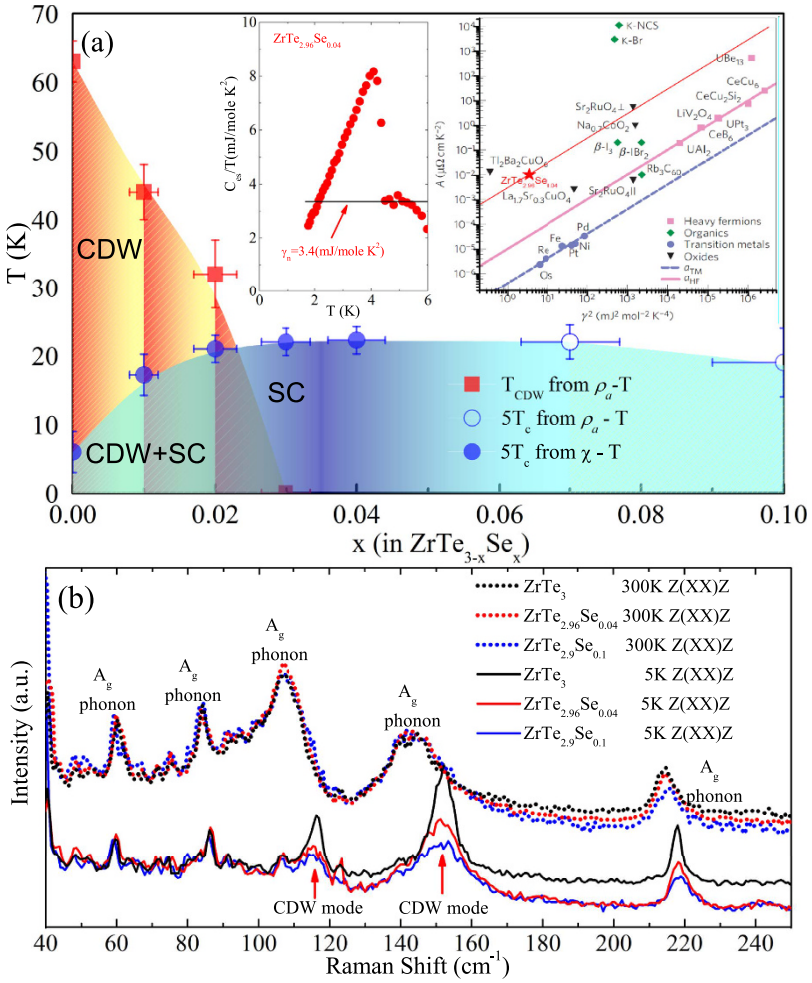

Figure 3. (**a**) The phase diagram of T_{CDW} and T_c versus Se doping content; insets show electronic specific heat and the Kadowaki - Woods ratio for $ZrTe_{2.96}Se_{0.04}$ (refs 26,27). The $a_{TM} = 0.4\,\mu\Omega$cm mol^2 K^2 J^{-2} and $a_{HF} = 10\,\mu\Omega$cm mol^2 K^2 J^{-2} are values seen in the transition metals and heavy fermions, respectively. Even though values of electron-electron scattering rate A and mass renormalization γ are smaller than in strongly correlated materials, it appears that the scaling A/γ^2 in $ZrTe_3$ is similar to Na_xCoO_2 and Sr_2RuO_4. (**b**) The normalized Raman scatering spetra for $ZrTe_3$, $ZrTe_{2.96}Se_{0.04}$, and $ZrTe_{2.9}Se_{0.1}$ measured at 5 K and 300 K with Z(XX)Z polarization. The two CDW modes at 115 cm^{-1} and 152 cm^{-1} are marked by arrows.

$\eta \approx 0.10(4)$ suggest different D_1 and D_2, i.e. approximately an order of magnitude different carrier mobilities in the two bands. This difference in the intraband diffusivities could be due to differences in scattering or effective masses[13,15].

Figure 3(a) depicts the $T(x)$ phase diagram of T_{CDW} and T_c versus Se content x for $ZrTe_{3-x}Se_x$. With increasing Se content x, the CDW order detected by a-axis resistivity anomaly is suppressed, vanishing around $x = 0.03$. SC T_c gradually increases up to the maximum $T_c = 4.4$ K around $x = 0.04$. With further increase in Se the superconducting T_c appears to have onset near 4 K, becoming much broader and with smaller shielding factor suggesting percolative nature of SC. Even though the sample with higher Se content cannot be grown at present, it is clear that the SC should decrease to $T_c = 0$ since $ZrSe_3$ is a band insulator with a band gap of 1 eV[17]. In contrast, Hf substitution on Zr site in $Zr_{1-x}Hf_xTe_3$ does not suppress the CDW order, and no SC is observed. This is different from

$IrTe_2$, in which only 5d Ir site substitution can suppress the charge/orbital order and induce SC[18]. The Hf doping does not alter the Te2/Te3 bands, which explains why Hf doping cannot suppress the CDW order and induce SC.

In what follows we compare the Raman signal of superconducting crystals to Raman signal of pure $ZrTe_3$ with long range CDW order. Figure 3(b) depicts the Raman spectra normalized to 86 cm^{-1} mode of $ZrTe_{3-x}Se_x$ measured at 5 K and 300 K with Z(XX)Z polarization for different Se content. Small Se doping should not change the phonon spectrum at the room temperature and indeed, the 300 K spectra nearly overlap with each other. As expected, the Raman spectrum of $ZrTe_3$ measured at 5 K is different from the one measured at 300 K. Two new modes appear around 115 cm^{-1} and 152 cm^{-1}, which we assign to CDW (CDW mode)[19,20]. Periodic lattice distortions in the CDW state will result in the new phonon modes below T_{CDW} and some (CDW modes) can be observed in the Raman spectra, for example in 1T-$TiSe_2$[21] and 2H-$NbSe_2$[22]. The 108 cm^{-1}, 140 cm^{-1} and 145 cm^{-1} modes are suppressed to low intensity with small temperature dependent shift at low temperature. The intensity of the two CDW modes 115 at cm^{-1} and 152 cm^{-1} becomes weaker for $x = 0.04$ and 0.1. It should be noted that CDW modes are detected outside the phase boundary of CDW order. The normalized amplitudes of the two CDW modes exist for $x = 0.04$ and 0.1, in crystals with no CDW signature in resistivity. This suggests a coexistence of superconductivity and CDW-related lattice distortions.

Discussion

Fermi surface of $ZrTe_3$ contains multiple bands with both flat and dispersive portions as well as substantial hybridization of high mobility chalcogen-derived bands with low mobility metal-derived bands[5]. We note that in $ZrTe_3$ CDW fluctuations affect the angular resolved photoemission spectral function $A(k, \omega)$ at temperatures above 200 K[23]. Scattering in such multiband CDW electronic system in the presence of local CDW fluctuations is dominated by scattering off collective CDW excitations below T_{CDW} [$\rho(T) \sim AT^2$; where A is a constant parameter] and the electron-phonon and impurity-like scattering off local CDW fluctuations above the T_{CDW} [$\rho(T) \sim aT + b$][24]. Both ρ_a and ρ_b are perfecly linear from about 60 K up to highest measured temperature of 300 K, whereas a $\sim T^2$ resistivity is observed from superconducting T_c up to about 80 K [Fig. 4(a,b)]. With suppression of the CDW order by pressure or doping, CDW mode should vanish[25], and indeed the absence of characteristic CDW-related hump is observed in resistivity. However as evident in Fig. 4(c), the signature of CDW mode in $ZrTe_{3-x}Se_x$ appears below about 100 K suggesting that the crystallographic vibration of the unit cell still senses CDW presence, but we speculate with no phase coherence.

The resistivity shows that electron-electron scattering due to CDW fluctuations dominates over the electron-phonon scattering and provides $\rho_a \sim AT^2$ temperature dependence with relatively high values of coefficient A. As a result, Kadowaki-Woods scaling A_a/γ^2 is comparable to $Tl_2Ba_2CuO_6$, Sr_2RuO_4 or $Na_{0.7}CoO_2$ [Fig. 3(a) insets][26–28]. In $ZrTe_3$, with increasing P, CDW order is first enhanced and reaches maximum T_{CDW} around 2 GPa[10], then decreases, vanishing around 5 Gpa, whereas superconducting T_c increases monotonically up to highest pressures. The phase diagram in Fig. 4b is different from this but Se could act as a chemical pressure due to its smaller size. Therefore slight increase in band filling of the quasi-1D Fermi surface sheet seen in pure $ZrTe_3$ under pressure could be the mechanism for the in-plane anisotropy and promotion of SC[29]. However, due to very small Se content (up to about 3 atomic %) and no appreciable change in the unit cell parameters, this would imply strong sensitivity of CDW to substitutions on Te site and possibly to disorder.

As doping increases beyond $x = 0.04$ the superconducing T_c forms a weak dome or plateau-like temperature dependence similar to $PrFeAsO_{1-x}F_x$[30]. Charge-mediated attraction is involved in both CDW and SC. For well nested Fermi surface long range CDW is stable and superconductivity is only filamentary along a axis arising in the Te2/Te3 $5p_x$ band[5,9]. With Se doping the CDW is no longer detected in scattering but dominant intraband interaction could ensure that patches of CDW still survive, as seen by Raman. The small Se substitution is unlikely to remove the nesting condition but may perturbe the long range phase coherence of CDW and consequently resistivity hump. Broad superconducting transition, small reduction of SC transition temperature and significant decrease in the superconducting volume fraction suggest that the percolative SC is independent of Se content once the CDW-related resistivity anomaly is absent.

The above discussion suggests a possibility for a CDW-fluctuation induced heavy-fermion-like mass enhancement contribution to mass tensor anisotropy[31]. Moreover, superconductivity on the verge of the breakdown of the long-range CDW order is reminiscent to magnetic fluctuation mediated superconductivity in copper oxide and heavy fermion materials where the magnetic order is tuned by doping or pressure to $T \rightarrow 0$ at the Quantum Critical Point[32–35].

Conclusion

In summary, we show that superconductivity in $ZrTe_{3-x}Se_x$ single crystals arises in the background of CDW fluctuations that contribute to significant anisotropy of the both normal state resistivity and the upper critical field in the superconducting state. The CDW fluctuations exist outside of the phase boundary of CDW order.

Methods

Single crystals of $ZrTe_{3-x}Se_x$ were grown via iodine vapor transport method[11]. The as grown single crystals can be easily cleaved along b-axis and c-axis, which usually produces needle- or tape- like crystals along b-axis in the ab plane (shown in inset of Fig. 1c). Elemental analysis was performed by energy-dispersive X-ray spectroscopy (EDS) on an FEI Helios Nanolab 600i to determine the Se content. The Se content in as grown crystal is found to be less than the content in the starting material; measured EDS values are presented in figures. Powder X ray diffraction confirms phase purity however there were no appreciable changes of the lattice parameters (below 0.002 Å for a, b and below 0.005 Å for c lattice parameter), as expected for atomic substitution of up to about 3%.

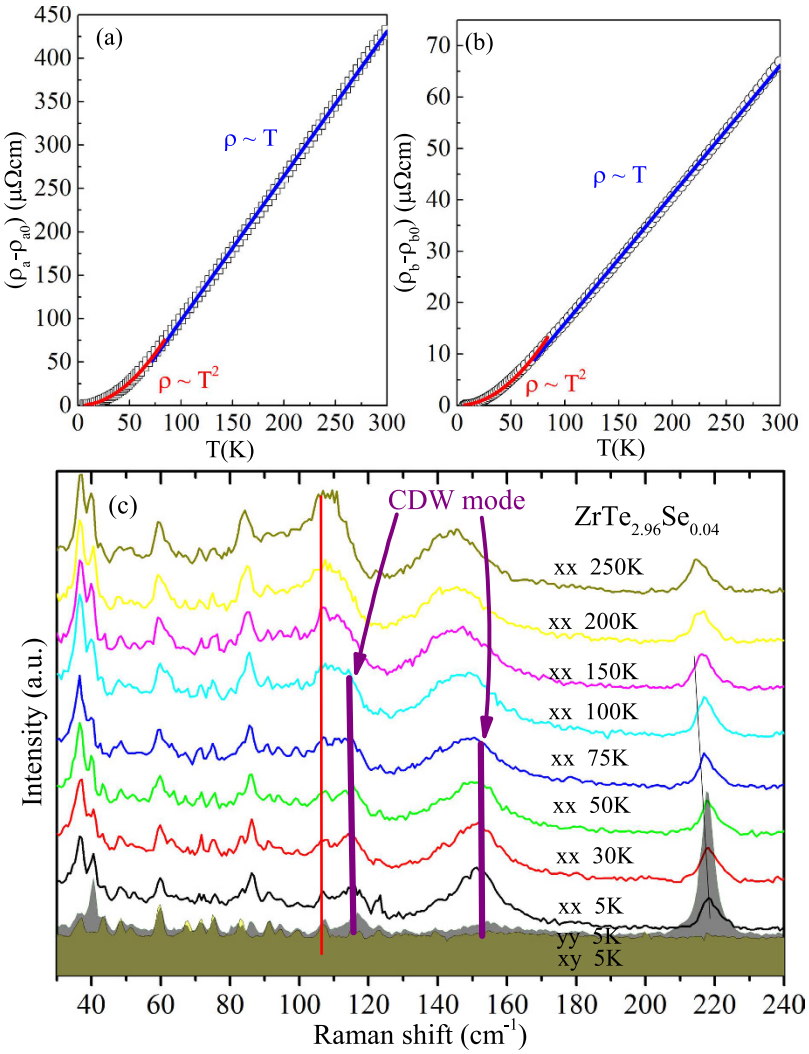

Figure 4. (**a**,**b**) The a- and b-axis resistivity fits of $ZrTe_{2.96}Se_{0.04}$. Below 63 K $\rho(T) \sim AT^2$ and above that temperature $\rho(T) \sim aT + b$ up to highest measured 300 K. The fitting parameters are $A_a = 0.0107(1)$, $A_b = 0.0019(1)$; $a_a = 0.250(1)$, $a_b = 1.66(1)$ and $b_a = -9.0(2)$ and $b_b = -68(1)$. (**c**) Raman scattering in $ZrTe_{2.96}Se_{0.04}$ where CDW mode can be traced below about 100 K.

The crystal size becomes smaller when the Se content x increases, reducing from about $3 \times 5\,mm^2$ for $x = (0–0.04)$ down to $1.5 \times 1.5\,mm^2$ in *ab*-plane for $x = 0.1$. Magnetization was measured in Quantum Design MPMS-XL-5. Resistance and magneto-resistance were measured by four probe method on Quantum Design PPMS-9 and PPMS-16. Raman spectra were measured on Horiba T64000, with excitation wavelength 647.4 nm and the power density was kept below 20 mW cm^{-2} in order to minimize the heating effects.

References

1. Gruner, G. *Density Waves in Solids* (Addison-Wesley, Reading MA 1994).
2. Gabovich, A. M., Voitenko, A. I. & Ausloos, M. Charge-density waves and spin-density waves in existing superconductors: competition between Cooper pairing and Peierls or excitonic instabilities. *Phys. Rep.* **367,** 583–709 (2002).
3. Torchinsky, D. H. *et al.* Fluctuating charge-density waves in a cuprate superconductor. *Nature Materials* **12,** 387–391 (2013).
4. Wilson, J. A. & Yoffe, A. D. The transition metal dichalcogenides discussion and interpretation of the observed optical, electrical and structural properties. *Adv. Phys.* **18,** 193–335 (1969).
5. Felser, C. *et al.* Electronic properties of $ZrTe_3$. *J. Mater. Chem.* **8,** 1787–1798 (1998).
6. Hoesch, M. *et al.* Splitting in the Fermi surface of $ZrTe_3$: A surface charge density wave system. *Phys. Rev. B* **80,** 075423, doi: 10.1103/PhysRevB.80.075423 (2009).
7. Eaglesham, D. J. *et al.* Electron microscope study of superlattices in $ZrTe_3$. *J. Phys. C* **17,** L697–L698 (1984).
8. Takahashi, S., Sambongi, T. & Okada, S. Conduction properties of $ZrTe_3$. *J. de Physique* **44,** 1733–1736 (1983).
9. Yamaya, K. *et al.* Mixed bulk-filament nature in superconductivity of the charge-density-wave conductor $ZrTe_3$. *Phys. Rev. B* **85,** 184513, doi: 10.1103/PhysRevB.85.184513 (2012).
10. Yomo, R. *et al.* Pressure effect on competition between charge density wave and superconductivity in $ZrTe_3$: Appearance of pressure-induced reentrant superconductivity. *Phys. Rev. B* **71,** 132508, doi: 10.1103/PhysRevB.71.132508 (2005).
11. Zhu, X. D., Lei, H. C. & Petrovic, C. Coexistence of bulk superconductivity and charge density wave in Cu_xZrTe_3. *Phys. Rev. Lett.* **106,** 246404, doi: 10.1103/PhysRevLett.106.246404 (2011).

12. Zhu, X. *et al.* Disorder-induced bulk superconductivity in $ZrTe_3$ single crystals via growth control. *Phys. Rev. B* **87,** 024508, doi: 10.1103/PhysRevB.87.024508 (2013).
13. Gurevich, A. Enhancement of the upper critical field by nonmagnetic impurities in dirty two-gap superconductors. *Phys. Rev. B* **67,** 184515, doi: 10.1103/PhysRevB.67.184515 (2003).
14. Werthamer, N. R. Helfand, E. & Hohenberg, P. C. Temperature and Purity Dependence of the Superconducting Critical Field, H_{c2}. III. Electron Spin and Spin-Orbit Effects. *Phys. Rev.* **147,** 295–302 (1966).
15. Jaroszynski, J. *et al.* Upper critical fields and thermally-activated transport of $NdFeAsO_{0.7}F_{0.3}$ single crystal. *Phys. Rev. B* **78,** 174523, doi: 10.1103/PhysRevB.78.174523 (2008).
16. Lei, Hechang *et al.* Multiband effects on β-FeSe single crystals. *Phys. Rev. B* **85,** 094515, doi: 10.1103/PhysRevB.85.094515 (2012).
17. Patel, K. *et al.* Optical and electrical properties of $ZrSe_3$ single crystals grown by chemical vapour transport technique. *Bulletin of Materials Science* **28,** 405–410 (2005).
18. Yang, J. J. *et al.* Charge-Orbital Density Wave and Superconductivity in the Strong Spin-Orbit Coupled $IrTe_2$:Pd. *Phys. Rev. Lett.* **108,** 116402, doi: 10.1103/PhysRevLett.108.116402 (2012).
19. Hu, Yuwen *et al.* Charge density waves and phonon-electron coupling in $ZrTe_3$. *Phys. Rev. B* **91,** 144502, doi: 10.1103/PhysRevB.91.144502 (2015).
20. Gleason, S. L. *et al.* Structural contributions to the pressure-tuned charge-density-wave to superconductor transition in $ZrTe_3$: Raman scattering studies. *Phys. Rev. B* **91,** 155124, doi: 10.1103/PhysRevB.91.155124 (2015).
21. Snow, C. S. *et al.* Quantum Melting of the Charge-Density-Wave State in 1T-$TiSe_2$. *Phys. Rev. Lett.* **91,** 136402, doi: 10.1103/PhysRevLett.91.136402 (2003).
22. Méasson, M. A. *et al.* Amplitude Higgs mode in the 2H-$NbSe_2$ superconductor. *Phys. Rev. B* **89,** R060503, doi: 10.1103/PhysRevB.89.060503 (2014).
23. Yokoya, T. *et al.* Role of charge-density-wave fluctuations on the spectral function in a metallic charge-density-wave system. *Phys. Rev. B* **71,** 140504, doi: 10.1103/PhysRevB.71.140504 (2005).
24. Naito, M. & Tanaka, S. Electrical transport properties in 2H-NbS_2, -$NbSe_2$, -TaS_2 and -$TaSe_2$. *J. Phys. Soc. Jpn.* **51,** 219–227 (1982).
25. Barath, H. *et al.* Quantum and Classical Mode Softening Near the Charge-Density-Wave Superconductor Transition of Cu_xTiSe_2. *Phys. Rev. Lett.* **100,** 106402, doi: 10.1103/PhysRevLett.100.106402 (2008).
26. Kadowaki, K. & Woods, S. B. Universal relationship of the resistivity and specific heat in heavy-fermion compounds. *Solid State Commun.* **58,** 507–509 (1986).
27. Jacko, A. C., Fjærestad, J. O. & Powell, B. J. A unified explanation of the Kadowaki-Woods ratio in strongly correlated metals. *Nature Physics* **5,** 422–425 (2009).
28. Nozières, P. & Pines, D. *The theory of Quantum Liquids* (Perseus Books, 1999).
29. Hoesch M. *et al.* Evolution of the charge density wave superstructure in $ZrTe_3$ under pressure. *Phys. Rev. B* **93,** 125102, doi: 10.1103/PhysRevB.93.125102 (2016).
30. Rotundu, C. *et al.* Phase diagram of the $PrFeAsO_{1-x}F_x$. *Phys. Rev. B* **80,** 144517, doi: 10.1103/PhysRevB.80.144517 (2009).
31. Murray J. M. & Tesanovic, Z. Theory of charge order and heavy-electron formation in the mixed-valence compound KNi_2Se_2. *Phys. Rev. B* **87,** 081103, doi: 10.1103/PhysRevB.87.081103 (2013).
32. Monthoux, P., Pines D. & Lonzarich, G. G. Superconductivity without phonons. *Nature* (*London*) **450,** 1177–1183 (2007).
33. Si, Qimiao & Steglich, F. Heavy fermions and quantum phase transitions. *Science* **329,** 1161–1166 (2010).
34. Sebastian, S. E. *et al.* Metal-insulator quantum critical point beneath the high T_c superconducting dome. *Proc. Natl. Acad. Sci. USA* **107,** 6175–6179 (2010).
35. Cano-Cortes, L., Merino J. & Fratini, S. Quantum critical behavior of electrons at the edge of charge order. *Phys. Rev. Lett.* **105,** 036405, doi: 10.1103/PhysRevLett.105.036405 (2010).

Acknowledgements

We thank Shile Zhang, Zhe Qu, Wenhai Song, Lanpo He, Shiyan Li for help on heat capacity measurements. Work at High magnetic field lab (Hefei) was supported by National Basic Research Program of China (973 Program), No. 2011CBA00111, and National Natural Science Foundation of China (Grants No. U1432251, 11204312, 11474289). Work at Brookhaven National Laboratory is supported by the US DOE under Contract No. DE-SC00112704.

Author Contributions

X.Z., C.P. and Y.Z. designed the experiments and wrote the draft. L.P., M.T. and Y.S. discussed the results and commented on the manuscript. Single crystals growth: X.Z. and L.L. SEM and EDS: H.D. Resistivity measurements and fits: W.N., K.W., L.L., X.Z. and C.P. Magnetization: L.L., Y.M. and Y.L. Raman: R.Z. and X.Z. Heat Capacity: J.Z.

Additional Information

Competing financial interests: The authors declare no competing financial interests.

How to cite this article: Zhu, X. *et al.* Superconductivity and Charge Density Wave in $ZrTe_{3-x}Se_x$. *Sci. Rep.* **6**, 26974; doi: 10.1038/srep26974 (2016).